PAPER

Magnetic-driven 3D-printed biodegradable swimming microrobots

To cite this article: Jingfan Chen et al 2023 Smart Mater. Struct. 32 085014

View the article online for updates and enhancements.

You may also like

- Design, analysis and experiments of a magnetic microrobot capable of locomotion and manipulation at water surfaces
 Yuanzhe He, Lefeng Wang, Qiang Li et al.
- Magnetic polymer composite artificial K E Peyer, E Siringil, L Zhang et al.
- Selective microrobot control using a thermally responsive microclamper for microparticle manipulation Gwangjun Go, Hyunchul Choi, Semi Jeong

Smart Mater. Struct. 32 (2023) 085014 (12pp)

https://doi.org/10.1088/1361-665X/ace1ba

Magnetic-driven 3D-printed biodegradable swimming microrobots

Jingfan Chen¹, Hanwen Hu¹ and Ya Wang^{1,2,3,4,*}

- ¹ J. Mike Walker '66 Department of Mechanical Engineering, Texas A&M University, College Station, TX 77843, United States of America
- ² Department of Electrical and Computer Engineering, Texas A&M University, College Station, TX 77843, United States of America
- ³ Department of Biomedical Engineering, Texas A&M University, College Station, TX 77843, United States of America
- ⁴ Department of Computer Science and Engineering, Texas A&M University, College Station, TX 77843, United States of America

E-mail: ya.wang@tamu.edu

Received 18 February 2023, revised 13 June 2023 Accepted for publication 26 June 2023 Published 4 July 2023



Abstract

A magnetic object subject to an external rotating magnetic field would be rotated due to the alignment tendency between its internal magnetization and the field. Based on this principle, 12 shapes of swimming microrobots around 1 mm long were designed and 3D-printed using biodegradable materials Poly (ethylene glycol) diacrylate (PEDGA). Their surface was decorated with superparamagnetic iron oxide nanoparticles to provide magnetic responsivity. An array of 12 permanent magnets generated a rotating uniform magnetic field (~100 mT) to impose magnetic torque, which induces a tumbling motion in the microrobot. We developed a dynamic model that captured the behavior of swimming microrobots of different shapes and showed good agreement with experimental results. Among these 12 shapes, we found that microrobots with equal length, width, and depth performed better. The observed translational speed of the hollow cube microrobot can exceed 17.84 mm s⁻¹ (17.84 body lengths/s) under a rotating magnetic field of 5.26 Hz. These microrobots could swim to the targeted sites in a simplified vessel branch. And a finite element model was created to simulate the motion of the swimming microrobot under a flow rate of 0.062 m s⁻¹.

Supplementary material for this article is available online

Keywords: magnetic microrobots, 3D-printed microrobot, permanent magnets array

1

(Some figures may appear in colour only in the online journal)

1. Introduction

Microrobots, like microorganisms, transport in a low Reynolds number regime, requiring motion patterns that differ from macroscale animals. According to Purcell's scallop theorem [1], nonreciprocal motion is necessary to obtain net movement or displacement in low Reynolds number Newtonian fluids, in which viscous forces dominate compared to inertial forces.

Wireless magnetic-driven microrobots have drawn extensive attention due to their potential for minimally invasive medical operations [2–4]. These microrobots are rationally designed to execute variety of tasks, such as drug delivery [5, 6] and sensing and diagnosis [7] by simulating the locomotion systems of microorganisms and forming their motion types under magnetic stimulation (for example, cork-screw forward by rotating magnetic field [8, 9], translation by magnetic field gradients [10], fluctuation by oscillating magnetic field [11, 12], reciprocating motion by periodic magnetic field [13]). Apart from breaking the symmetry from the geometrical point of view,

^{*} Author to whom any correspondence should be addressed.

another strategy to overcome the Scallop theorem and induce translational movement is introducing a physical boundary to break the spatial symmetry. Navigation on the surface of the blood vessels is advantageous because of decreased flow velocities. Inspired by leukocytes or neutrophils, which locomote in vascular channels along the vessel walls due to a relatively low flow velocity therein, magnetic surface walkers have been proposed for target delivery in confined microchannel environments [14–17]. Such locomotion can be achieved by magnetically activating a magnetic microrobot near a surface [18]. For example, crawling locomotion was achieved through Kresling origami-induced in-plane contraction caused by a magnetic actuation [19]. Stick-slip motion in the rectangular magnetic microrobot was induced by periodically varying magnetic fields [20]. An alternate form of locomotion was explored using a tumbling microrobot with a dumbbell structure with two oppositely polarized magnetic bell parts [21, 22]. The tumbling working mechanism, actuated with an alternating magnetic field, avoids the relative motion and constant contact against the surface, achieving effectiveness with their ability to access previously unreachable body areas.

To fabricate magnetic microrobots with desired architecture, various microfabrication techniques have been used, such as template-assisted electrodeposition [23], laser lithography [5, 11, 24, 25], glancing angle deposition [26, 27] and 3D printing [7, 9]. The magnetic section, such as Ni thin films and neodymium-iron-boron permanent magnets, was deposited during the fabrication. Among these fabrications, 3D printing provides a feasible approach to fabricating microrobots with predesigned shapes. In addition, there have been several studies that have utilized magnetic feedstock to produce highperformance bonded magnets using additive manufacturing. These studies demonstrate the potential of magnetic feedstock in the production of high-performance magnets with enhanced magnetic properties. The use of additive manufacturing techniques in combination with magnetic field alignment methods allows magnets with complex shapes and tailored magnetic properties, which can benefit a range of applications [28–30].

To actuate magnetic microrobots, a magnetic system usually consists of either an electromagnets [31–34] or permanent magnets as the source of the magnetic field [35–37]. Electromagnets-based magnetic actuation systems generate magnetic fields from flowing currents through coils. A typical electromagnet is formed by winding insulated copper wires around a ferromagnetic core, which concentrates and amplifies the magnetic field. Triaxial circular Helmholtz coils are the most commonly used for actuating magnetic microrobots [26, 38]. While permanent magnets are easily obtainable and provide strong magnetic strength without a high current supply. The distribution and strength of the magnetic field depend on its geometrical shape and size.

Magnetic microrobots have great potential to deliver vehicles [39, 40] for magnetic nanoparticles (NPs) [41]. In our previous work, we have conducted both *in vitro* and *in vivo* experiments to study the application of superparamagnetic iron oxide (SPIO) NPs as drug carriers, which did not induce significant toxicity or inflammation in different cells and mice [42–45]. However, the rapid decay of magnetic field strength

with distance from its source creates a significant challenge for controlling SPIO NPs [36, 45]. One fundamental limitation of the magnetic force-driven principle is that the external magnetic fields decrease roughly volumetrically in strength as distance increases between the magnetic objects and the source of the area.

To improve the controllability of SPIO NPs, in this paper, we decorated SPIO NPs on the surface of magnetic-driven swimming microrobots. The microrobots are first 3D-printed and immersed in a water suspension of SPIO NPs for magnetic actuation. A custom magnet array with 12 permanent magnets and two DC motors creates a uniform rotating magnetic field inside the working space with magnetic strength about 100 mT (figure 1(a)). The difference in the orientation between the microrobot's internal magnetization and that of a rotating magnetic field induces magnetic torque on the microrobot, making it tumble forward end-over-end (figure 1(b)). Next, we show the motion of the microrobot under varying field rotational frequencies and demonstrate the ability of two-dimensional controllability of the microrobot. Finally, we present a comprehensive dynamic model of the microrobot and its interactions with the magnetic fields. Such a model is necessary to understand the nature of the microrobot's motion and thus can be used as a tool to optimize its geometry.

2. Results and discussion

2.1. Design and fabrication

The microrobot was 3D printed by using StemakerTM Model D, which has a resolution of 10 μ ms in the X and Y directions and 100 μ ms in the Z direction, allowing for the creation of features as small as 10 μ ms in the X and Y directions and layer heights as small as 100 μ ms in the Z direction. However, achieving precise prints depends on the exposure time and light intensity. The 3D model was designed in Solidworks and sliced into a series of digital images. These images are then projected onto the photopolymerizable materials, which are loaded on a motorized stage. Areas illuminated by UV light (405 nm) crosslink within seconds while leaving the dark regions uncross-linked, forming a patterned layer in a specific polymerization plane. We used Poly (ethylene glycol) diacrylate (PEDGA Mn = 700 Da, Sigma) with the photoinitiator of 2% irgacure 819 Phenylbis (2,4,6-trimethyl benzoyl) phosphine oxide (Sigma). PEGDA is a synthetic polymer that is not biodegradable in the traditional sense. However, PEGDA can be biodegraded through other means, such as hydrolysis, which involves breaking down the polymer chain through a reaction with water. This process can occur over time, particularly under certain conditions such as exposure to heat or certain enzymes. Browning et al [46] reported that the degradation mechanism of PEGDA hydrogels in vivo is primarily through hydrolysis of the end-group acrylate esters, which results in the cleavage of PEG chains from the hydrogel network. Stillman et al [47] found that the PEDGA-based hydrogel NPs degrade slowly in vitro, with more rapid degradation in vivo due to the presence of enzymes in the body. Besides, PEDGA displays essential features such as biocompatibility,

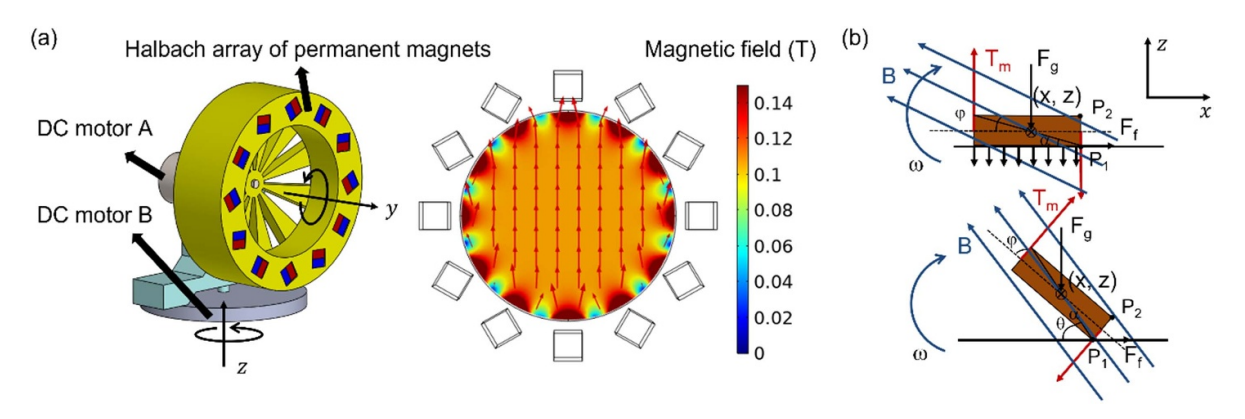


Figure 1. (a) The Schematic of the permanent magnet array design and the simulated 2D magnetic field profile shows the uniform magnetic field in the center. (b) Mechanism of the tumbling microrobot. The dashed lines represent the internal magnetic alignment, and its arrow represents the magnetic alignment's direction. The adhesive force is distributed uniformly over the surface area. The adhesive force is almost zero when the microrobot has line contact with the surface.

biodegradability, and stealth, making it versatile for various bio-applications. For photopolymerization-based 3D printing, it is critical to determine the appropriate light exposure. Underexposure cannot photopolymerize the material, while overexposure may cause unwanted polymerization [48]. To achieve a high resolution and printability for the microrobot, 4 different light intensities (10%, 20%, 40%, and 60%) were chosen to print hollow cylinder and helix structures. Figure 2 shows the schematic of microrobots (Hollow Cylinder 1, Hollow Cylinder 2, Helix 1, and Helix 2) with different light intensities by Motic AE2000 inverted biological microscope. The designed and printed sizes are listed in table 1. For the light intensity of 10%, we failed to print the structures, which means the light exposure is insufficient. For the light intensity of 20%, although it has the minimum errors to print the hollow cylinder structures, it failed to print helix structures. We found that the structures swelled for the light intensity of 60%, suggesting overexposing. Thus, the print speed was set to 0.05 mm s^{-1} , and the light intensity was set to 40% for the following microrobots.

A total of 12 types of microrobots were designed and fabricated, including three series: (1) hollow series, (2) U-shape series, and (3) complex series. In the hollow series, the performance of two different shapes, hollow cube and hollow cylinder, and the effect of varying diameters of the hollow cylinder was compared. In the U-shape series, four different shapes, square, rolling, long, and short U-shapes, were compared. Finally, complex structures were further designed and fabricated to test the applicability of our theoretical model. To decorate PEDGA architecture with SPIO NPs for magnetic actuation, the microrobot was immersed in a water suspension of 200 mg ml⁻¹ SPIO NPs (Ferrotec EMG 304) for 24 h [9]. The color of the microrobots after coating exhibits a consistent hue, which is considered acceptable in terms of uniformity for the 1 mm size range (figure S1). The SPIO NPs in this paper are negatively charged, which makes them stable in aqueous solutions. The adsorption of SPIO NPs onto PEGDA surfaces is hypothesized to occur through a complex interplay of molecular interactions, including hydrogen bonds, electrostatic interactions and van der Waals forces. Another possible mechanism is diffusion-controlled absorption, in which the SPIO NPs diffuse into the hydrogel matrix through the spaces between the polymer chains. Further research is needed to fully understand the mechanisms of SPIO NPs adsorption on PEGDA surfaces and to develop improved PEGDA-based magnetic microrobots. We conducted three measurements on both Hollow Cylinder 1 and Cylinder 2 before and after the coating process (figure S2). The results consistently show that the outer diameter of both structures increased by 10% after the coating.

2.2. Magnetization orientation of microrobots

SPIO NPs become a single magnetic domain and exhibit high magnetic susceptibility properties in an external magnetic field, thereby introducing magnetization on microrobots. Unlike ferromagnetic materials such as Fe, Ni, and Co, SPIO NPs provide a faster and stronger magnetic response with negligible coercivity and remanence. The magnetization orientation of microrobots influences their motion. The tumbling motion (rotation around its short axis) occurs near a surface under an external rotating magnetic field when a microrobot is magnetized along its long axis. However, when the microrobot is magnetized along its short axis, it rolls (rotates around its long axis) on the surface under the same applied rotating magnetic field. SPIO NPs are highly magnetic particles that exhibit unique behavior in the presence of an external magnetic field. When exposed to a magnetic field, SPIO NPs become magnetized and align themselves with the direction of the field. This property makes them a valuable magnetic material to create magnetic microrobots without needing pre-magnetization along different axes. Figures 3–5 show the magnetization orientation of the different series of microrobots along the z-axis.

2.3. Propulsion mechanism

The microrobot will experience both a torque and a force within a magnetic field. This magnetic torque is proportional to the magnetic field strength and acts in a direction to bring the

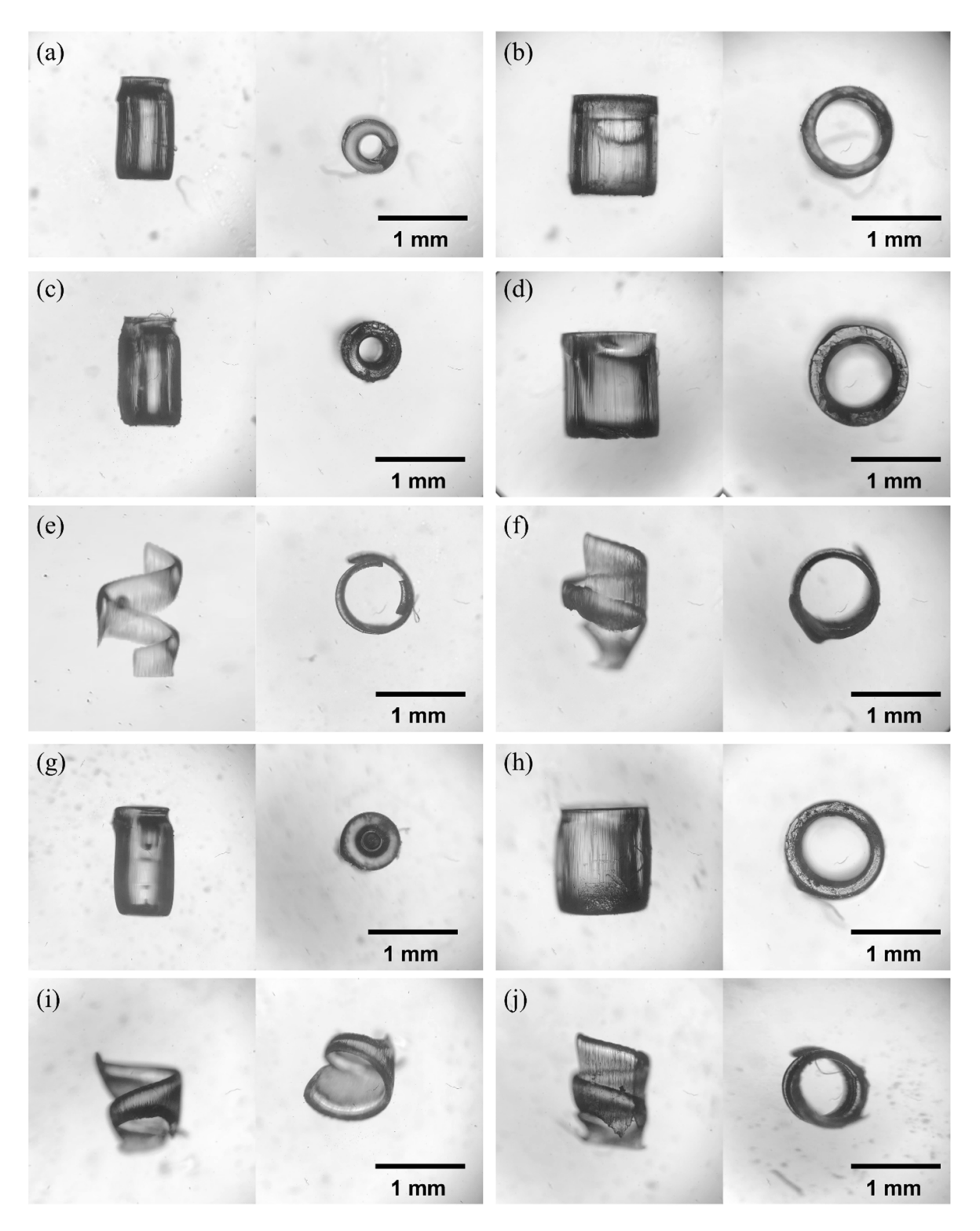


Figure 2. The optical microscopy images (side and bottom views) of microrobots with different light intensities. 20% light intensity: (a) Hollow Cylinder 1 and (b) Hollow Cylinder 2; 40% light intensity: (c) Hollow Cylinder 1, (d) Hollow Cylinder 2, (e) Helix 1 and (f) Helix 2; 60% light intensity: (g) Hollow Cylinder 1, (h) Hollow Cylinder 2 (i) Helix 1 and (j) Helix 2.

internal magnetization of the microrobot into alignment with the field. The magnetic force is proportional to the magnetic field's gradient and moves the microrobot to a local maximum. The torque can be expressed as:

$$T_{\rm m} = VM \times B \tag{1}$$

and the magnetic force is:

$$\boldsymbol{F}_{\mathrm{m}} = V(\boldsymbol{M}\nabla)\boldsymbol{B} \tag{2}$$

where M [A m⁻¹] is the magnetization of the microrobot and B [T] is the external magnetic field. The tumbling

Table 1. The design and print size of microrobots with different light intensities.

	Hollow Cylinder 1			Hollow Cylinder 2		
	Length (mm)	Diameter (mm)	Thickness (mm)	Length (mm)	Diameter (mm)	Thickness (mm)
Design	1.000	0.500	0.100	1.000	1.000	0.100
20%	1.151	0.555	0.151	1.115	1.021	0.115
40%	1.198	0.636	0.135	1.198	1.073	0.167
60%	1.208	0.646	0.167	1.198	1.083	0.146
		Helix 1			Helix 2	
	Pitch (mm)	Cross section height (mm)	Cross section width (mm)	Pitch (mm)	Cross section height (mm)	Cross section width (mm)
Design	0.670	0.160	0.080	0.500	0.160	0.080
40%	0.690	0.352	0.074	0.609	0.346	0.082
60%	0.700	0.370	0.083	0.599	0.388	0.105

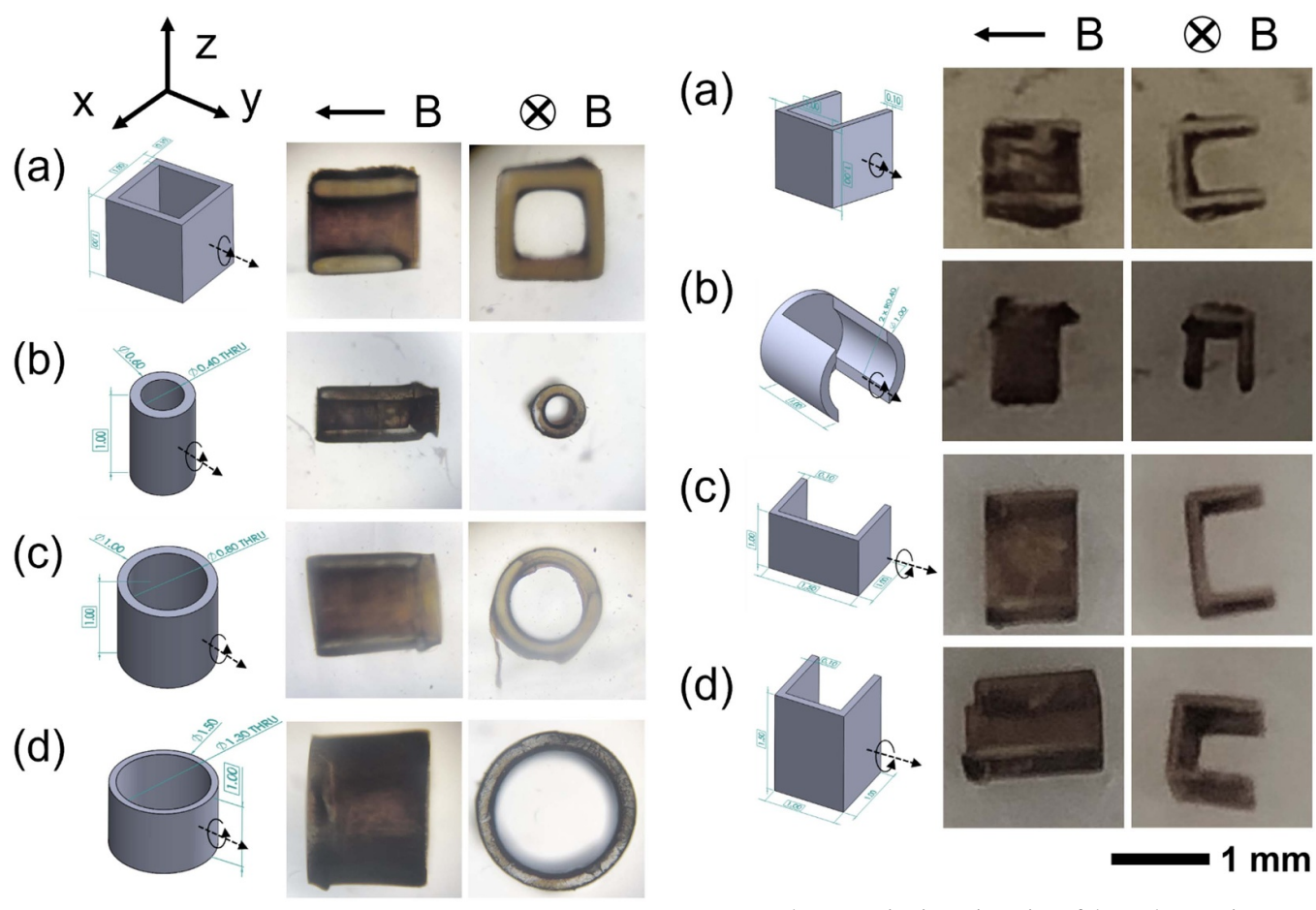


Figure 3. The magnetization orientation of the hollow series microrobots (a) Hollow Cube; (b) Hollow Cylinder 1, (c) Hollow Cylinder 2, and (d) Hollow Cylinder 3.

motion of the microrobot discussed in this paper is achieved by providing rotating magnetic fields from the magnetic applicator in figure 1(a). A Halbach array of 12 magnets (NdFeB, grade N52, core strength of 1.48 T, dimensions $12.7 \times 12.7 \times 25.4$ mm, K&J Magnetics, Inc.) was designed

Figure 4. The magnetization orientation of the U shape series microrobots (a) Square U; (b) Rolling U, (c) Short U, and (d) Long U.

to generate a uniform magnetic field inside the center. By rotating this Halbach array through a DC motor (motor A), a rotating uniform magnetic field can be generated with a magnetic strength of about 100 mT as simulated by COMSOL Multiphysics. In addition, the bottom of the applicator was attached to another DC motor (motor B), which enable this magnetic field to control the forward direction of the tumbling microrobot.

1 mm

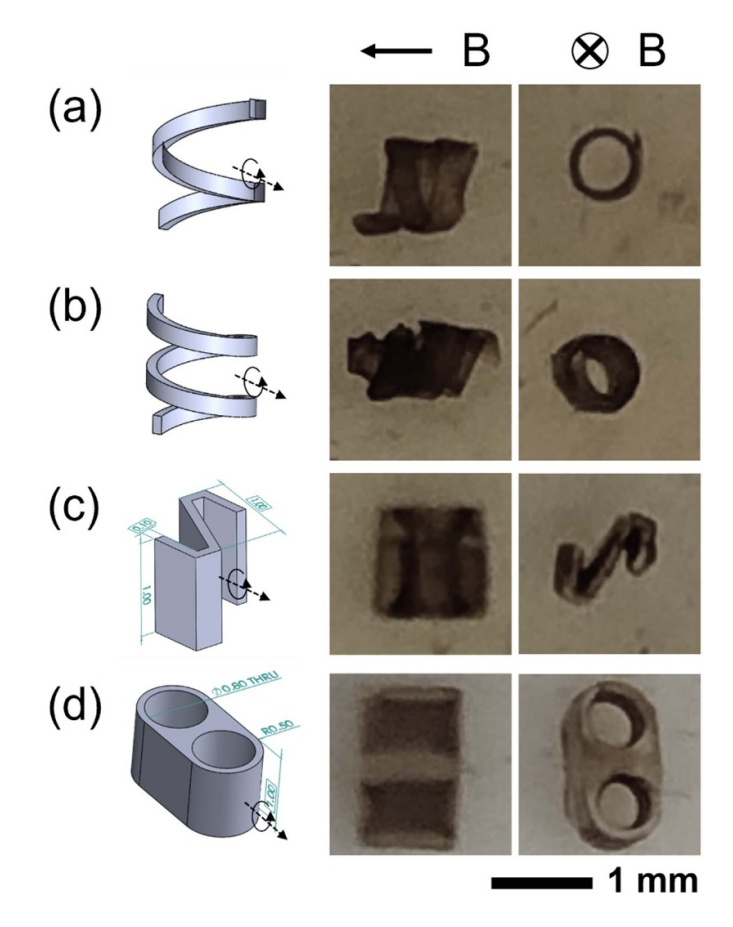


Figure 5. The magnetization orientation of the other shape series microrobots (a) Helix 1; (b) Helix 2 (c) Z-shape and (d) two-hollow Cylinder.

2.4. Theoretical analysis of the swimming microrobot

To simulate the dynamics of the swimming microrobot, we assume it is an isotropic rectilinear solid and restrict modeling to a side-view of the microrobot in the x-z plane, shown in figure 1(b). The microrobot's position (x, z) is taken at its center of mass (COM) and has an orientation angle θ measured clockwise from the ground, a distance r from its COM to a corner, and an angle $\alpha = \tan^{-1}\frac{D}{L}$ determined from geometry. As the magnetic applicator rotates, the driving torque is generated, lifting the microrobot to tumble. The microrobot must follow the rotating magnetic field before another tumble is possible. The translational velocity of the microrobot grows with the rotating frequency (ω) of the magnetic field until a stepout frequency is reached. Beyond this step-out frequency, the available magnetic torque is no longer sufficient to keep the microrobot tumbling to follow the rotating magnetic field.

The microrobot performs periodic tumbling motions. The microrobot is first assumed pinned to the point P_1 , where $0 \le \theta \le \frac{\pi}{2}$, then is pinned to the point P_2 , when. The kinematics of the microrobot can be approximated as:

$$\dot{x} = \begin{cases} r\sin(\theta + \alpha)\dot{\theta}, & 0 \leqslant \theta \leqslant \frac{\pi}{2} \\ r\sin(\theta - \alpha)\dot{\theta}, & \frac{\pi}{2} \leqslant \theta \leqslant \pi \end{cases}$$
(3)

$$\dot{z} = \begin{cases} r\cos(\theta + \alpha)\dot{\theta}, & 0 \leqslant \theta \leqslant \frac{\pi}{2} \\ r\cos(\theta - \alpha)\dot{\theta}, & \frac{\pi}{2} \leqslant \theta \leqslant \pi \end{cases}$$
 (4)

Here, a dot over a symbol means the time derivative.

Due to the uniformity of the applied rotating magnetic field, a negligible magnetic force was exerted on the microrobot. Assuming there is no sliding motion, the governing equation of the tumbling microrobot can be expressed as:

$$I\ddot{\theta} = T_{\rm m} - \tau_{\rm d} - F_{\rm g}r \times \cos(\theta + \alpha) - F_{a}\frac{L}{2} \quad . \tag{5}$$

The magnetic torque applied on the microrobot $T_{\rm m} =$ $V_{\rm m} |M| |B| \sin \varphi$, where $\varphi = \omega t - \theta$ is the magnetic alignment offset angle. The drag torque per unit length L of a cylinder rotating close to a wall is given by [49], $\frac{\tau_d}{L} = \frac{4\pi u_d \dot{\theta} r^2}{\sqrt{1-k^2}}$, where $k = \frac{r}{r+d_0}$, d_0 depicts the gap distance between the microrobot and surface and u_d is the dynamic viscosity of water. The volumetric vertical force of the microrobot $F_g = \rho_{\rm SPIO} g V_{\rm m} +$ $\rho_{\text{PEGDA}}gV - \rho_{\text{water}}g(V_{\text{m}} + V)$ is the combined action of the weight of the microrobot and its buoyancy. Here, V is the volume of the microrobot without SPIO NPs coating, ρ_{SPIO} , ρ_{PEGDA} , ρ_{water} are the density of the SPIO NPs, PEGDA and water, respectively. $F_a = C_a S$ is the adhesive force between the microrobot and the surface when it rests, where C_a is the coefficient of adhesive force, S is the contact area. Based on the governing equation, the design of a microrobot determines its tumbling motion. A smaller moment of inertia will result in a faster rotation for a given torque, meaning that a microrobot with a smaller moment of inertia will require less torque to achieve the same angular acceleration than a structure with a larger moment of inertia. For a uniform structure, the moment of inertia is directly proportional to its length. Therefore, a longer microrobot will have a more significant moment of inertia than a shorter one, assuming they have the same mass and uniform distribution of mass. However, a longer length will also result in more enormous drag torque, requiring more magnetic torque to lift it up. The equation can be numerically solved by using MATLAB software.

Table 2 shows the parameters used in the theoretical analysis of the motion of the microrobots. The subscript of 0 means the properties of the microrobot before coating SPIO NPs.

Figure 6(a) displays several frames from one 60 frame per second experimental video of Helix 2 in the x-y plane exhibiting tumbling motion when actuated by a rotating magnetic field at 0.42 Hz. Figure 6(b) depicts the simulated motion (rotation degree) of Helix 2 in the x-y plane. Since the microrobot's structure is assumed to be symmetric about the x-axis in the simulation, implying that the dimensions along the y and z directions are equal, the simulation results agree with the experimental observations.

2.5. Microrobots performance

To evaluate the performance of microrobots and calculate their translational velocity, the microrobot was detected using OpenCV and Python. Basically, we first removed the noise

Parameters	Symbol	Value	
Radius of SPIO NP	R	5 (nm)	
Volume of SPIO NP	$V_{ m SPIO}$	$5.23 \times 10^{-25} (\text{m}^3)$	
Density of SPIO NP	$ ho_{ ext{SPIO}}$	$5240 (\text{kg m}^{-3})$	
Single SPIO mass	$m_{ m SPIO}$	$2.74 \times 10^{-21} (kg)$	
Density of PEGDA	$ ho_{ ext{PEGDA}}$	$1120 (\text{kg m}^{-3})$	
Density of water	$ ho_{ m water}$	$1000 (\text{kg m}^{-3})$	
Rotating magnetic field	B	0.1 (T)	
Magnetization of SPIO	M	$21936.75(\mathrm{A}\;\mathrm{m}^{-1})$	
Coefficient of adhesive force	C_a	$1.19 (\mathrm{N \ m}^{-2})$	
Number of SPIO NPs in microrobot	n	$S_0/(\pi R^2)$	
Magnetic part volume	$V_{ m m}$	$n \times V_{\rm SPIO}~({\rm m}^3)$	
Total mass	m	$m_0 + n \times m_{\rm SPIO}$ (kg)	
Moment of inertia	I	$I_0/m_0 \times m (\mathrm{kg m}^2)$	

Table 2. Parameters for theoretical analysis.

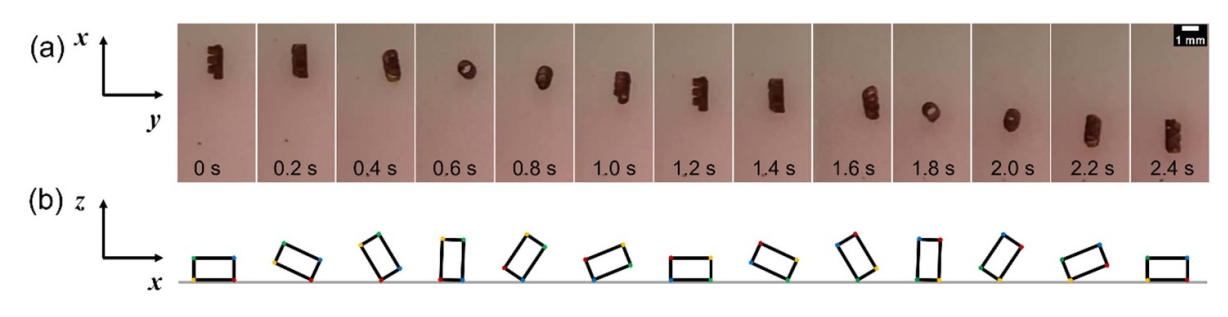


Figure 6. Frames extracted from the video recording of Helix 2 under the rotating magnetic field at 0.42 Hz, compared to the simulated results. (a) The microrobot is initially rest in the surface. When the magnetic field rotates, the microrobot tumbles to align the magnetic field. The contact points keep changing, and the microrobot moves forward. (b) The simulated responses of the rotation degree. The contact points change from red, blue, green to yellow.

in the video with Gaussian filter. This step slightly smoothed the images to reduce the effects of obvious noise on the edge detector. And then the edge of the microrobot was detected by Canny edge detection algorithm. Thus, the translational speed and the offset degree of the microrobot can be calculated. The real time speed and offset degree of Helix 2 under the rotating magnetic field at 3.2 Hz (figure 7) indicated that it translated forward with an approximately uniform speed.

The average translational speeds of the hollow series, Ushape series, and other shape series microrobots under varying field rotational frequencies were plotted in figures 8–10. The translational speed of the microrobots increases roughly linearly at the low frequency as the rotational frequency of the external field increases, indicating that the microrobots tumble without slipping. However, the theoretical results show a faster translational speed at higher field rotational frequencies. This difference indicated slippage of the microrobot while tumbling, and the slippage increases at higher rotating frequency. One possible explanation for the moderate match between theory and experiment is the simplification of the theoretical model. In reality, the friction and adhesive force between the microrobot and the surface is more complex and may need to be fully captured in the theoretical model, which can affect the complex dynamics of the microrobots in the experiments. Additionally, experimental conditions and measurement errors may influence the discrepancies between the theoretical and experimental results. The magnetic applicator introduces vibrations at higher frequencies, leading to non-uniform magnetic fields and mismatches with the theoretical study. However, despite these limitations, the theoretical model can still provide valuable insights into the motion of tumbling microrobots and help to optimize structure design. Table 3 lists the maximum translational speeds and step-out frequencies of different microrobot shapes.

For the hollow series microrobots, a maximum translational speed of 17.87 mm s $^{-1}$ was measured for Hollow Cube at the frequency of 5.26 Hz, and 10.40 mm s $^{-1}$ for Hollow Cylinder 1 at 4.50 Hz, 16.84 mm s $^{-1}$ for Hollow Cylinder 2 at 8.00 Hz, 12.62 mm s $^{-1}$ for Hollow Cylinder 3 at 6.60 Hz. The theoretical results agree well with the experimental results, especially for the Hollow Cube microrobot. The reason could be that the microrobot was treated as an isotropic rectilinear solid in the theoretical model, and the other shape was not considered.

For the U-shape series microrobots, a maximum translational speed of 17.29 mm s⁻¹ was measured for Square U at the frequency of 7.64 Hz, and 5.09 mm s⁻¹ for Rolling U at 1.59 Hz, 13.52 mm s⁻¹ for Short U at 5.21 Hz, 15.94 mm s⁻¹ for Long U at 4.01 Hz. Due to the simplification of the structure in the theoretical model, the hypothetical results of Square U and Rolling U microrobots are similar. However, in practice, although the Rolling U microrobot has a minor moment of inertia, the rolling structure makes it prone to slippage. The

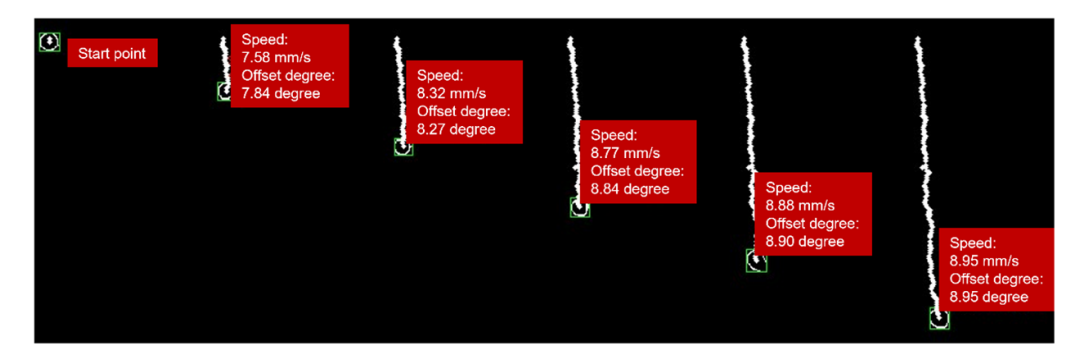


Figure 7. Frames extracted from the video after detecting the motion of Helix 2 under the rotating magnetic field at $3.2 \, \text{Hz}$ with OpenCV (time step = $0.5 \, \text{s}$).

Table 3. The maximum speed and frequency for different shapes of microrobots.

Microrobots	Maximum speed (mm s ⁻¹)	Step-out frequency (Hz)
Hollow series		
Hollow Cube	17.87	5.26
Hollow Cylinder 1	10.40	4.50
Hollow Cylinder 2	16.84	8.00
Hollow Cylinder 3	12.62	6.60
U series		
Square U	17.29	7.64
Rolling U	5.09	1.59
Short U	13.52	5.21
Long U	15.94	4.01
Other shape series		
Helix 1	9.04	3.95
Helix 2	7.95	3.00
Z-shape	13.87	5.11
2 Hollow Cylinder	14.12	4.41

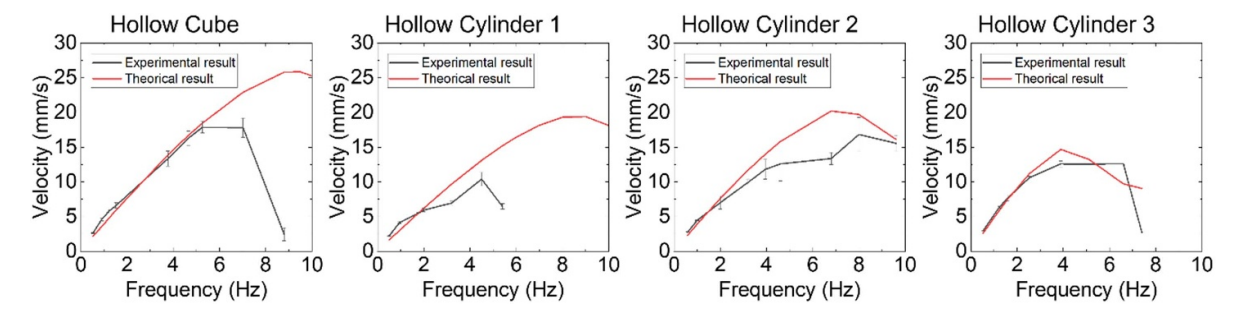


Figure 8. The experimental and theoretical average translational speed under varying field rotational frequencies of the hollow series microrobots.

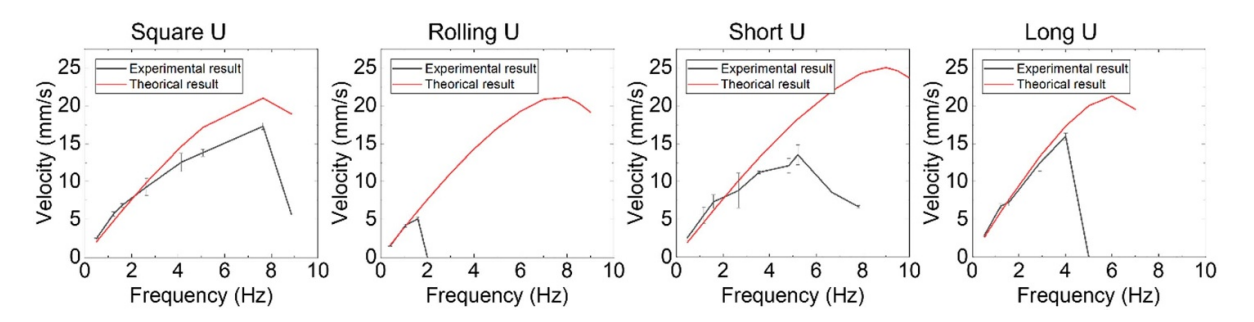


Figure 9. The experimental and theoretical average translational speed under varying field rotational frequencies of the U-shape series microrobots.

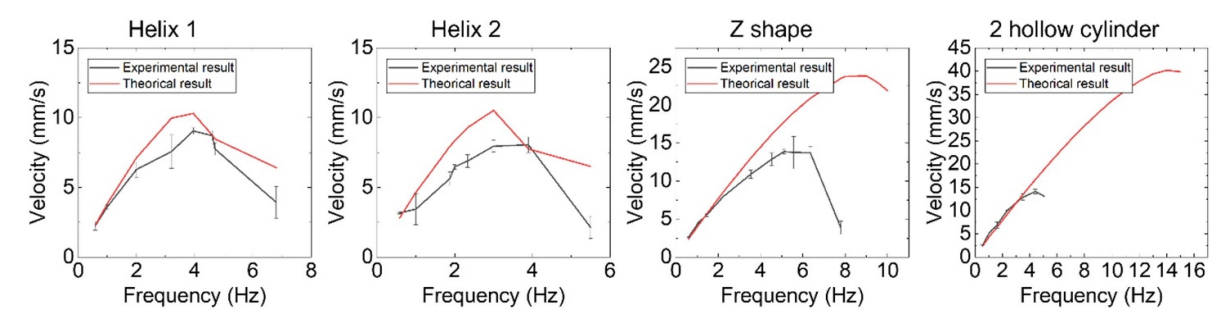


Figure 10. The experimental and theoretical average translational speed under varying field rotational frequencies of the other shape series microrobots

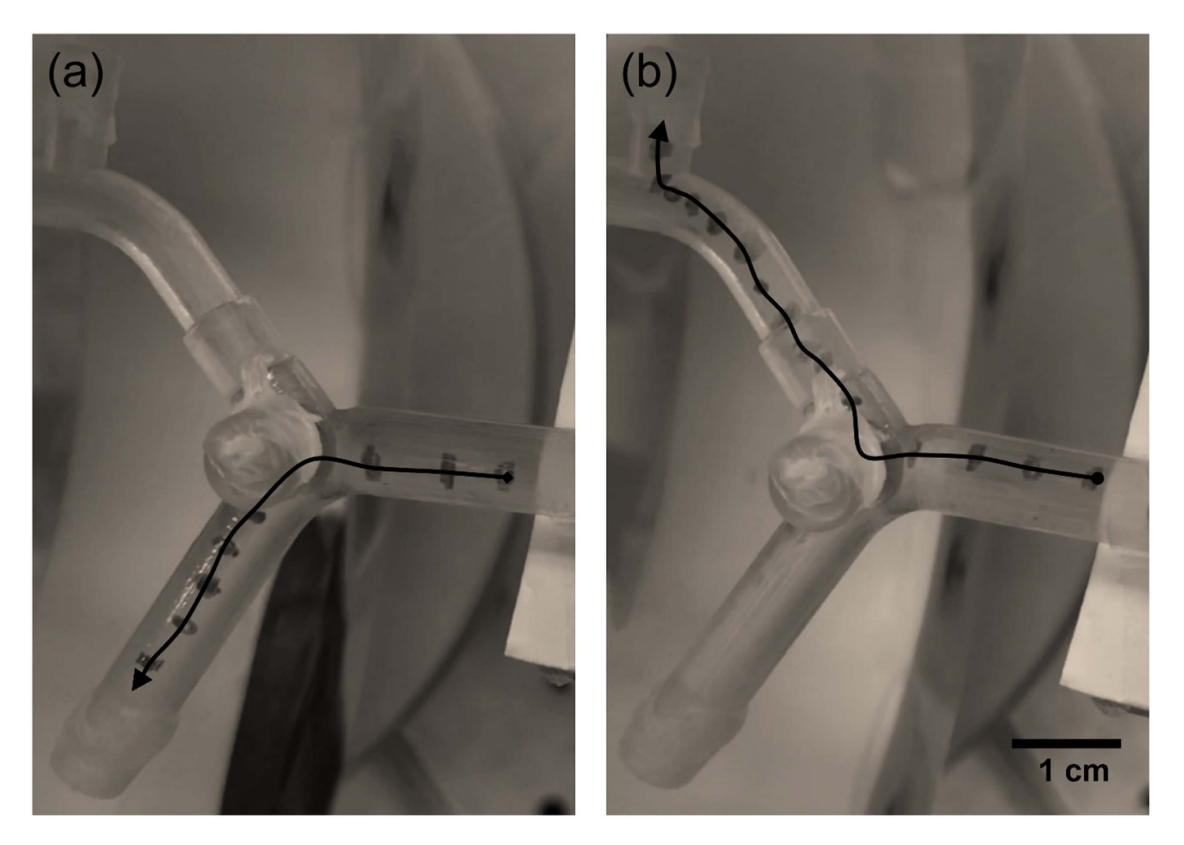


Figure 11. Frames extracted from the video recording of the helix 2 transport for arriving at the (a) middle cerebral arteries (MCA) and (b) Anterior cerebral arteries (ACA).

external magnetic field fails to align the magnetization of the microrobot, resulting in a low step-out frequency.

For the other shape series microrobots, a maximum translational speed of $9.04~\rm mm~s^{-1}$ was measured for Helix 1 at the frequency of $3.95~\rm Hz$, and $7.95~\rm mm~s^{-1}$ for Helix 2 at $3.00~\rm Hz$, $13.87~\rm mm~s^{-1}$ for Z-shape at $5.11~\rm Hz$, $14.12~\rm mm~s^{-1}$ for 2 Hollow Cylinder at $4.41~\rm Hz$. Interestingly, in the experiments, the 2 Hollow Cylinder microrobot appears to wobble due to the inconsistency of SPIO NPs in its hole surface. Thus, it fails to follow the magnetic field at high frequencies.

Among these 12 shapes of microrobots, we found that the microrobots with equal length, width, and depth, such as Hollow Cube, Hollow Cylinder 2, Square U had better performance. Since the entire surface of microrobots are coated with SPIO NPs, some areas that are perpendicular to the magnetic field and generate resisting torque during the tumbling.

Thus, theoretical analysis of some structures still suggested that the speed of microrobots would continue to increase as the rotating frequency increases. Overall, the theorical model can predict the motion of the tumbling microrobot of different shapes, thus can be used to guide the design of microrobots.

2.6. Navigation of the microrobot

To demonstrate the two-dimensional controllability of the microrobot, Helix 2 was driven on a 3D printed circle of Willis [36]. The microrobot's motion was confined to the *x-y* plane. Linear propulsion is achieved by a rotating magnetic field that is driven by the DC motor A, while the direction in *x-y* plane was controlled by the motor B. By simultaneously rotating the magnetic applicator about the *y* and *z* axes for the tumbling and turning of the microrobot respectively, the microrobot is able

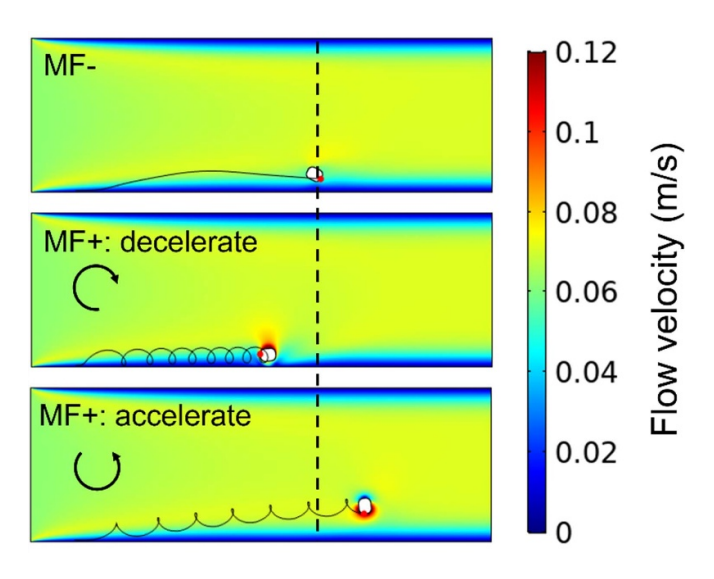


Figure 12. Simulation result of the motion of microrobot under the flow speed of 0.062 m s^{-1} . The line shows the trajectory of the microrobot.

to translate in two dimensions. As shown in figure 11 (frames captured per 2 s), Helix 2 can be transport through the either ACA or MCA under the rotating frequency of 0.5 Hz.

Currently, the controllability of small-scale robots is limited in stagnant fluidic environments. The drag force of substantial fluidic flows may disrupt the propulsion capability and disturb the motion control of a microrobot, resulting in negative net motion or uncontrolled locomotion in the viscous biofluids [2]. To date, it is still unclear how to make microrobots resist the variable flow rate. Without overcoming this problem, the microrobots could not pass through the blood vessels in a controllable manner to arrive at the targeted location. Here, we conducted a simulation in COMSOL Multiphysics to test the motion of the tumbling microrobot under a flow rate of $0.062 \,\mathrm{m \, s^{-1}}$ (the general blood flow rate of the adult mice) [50]. A clockwise or counterclockwise rotating magnetic field (MF+) has an effect on the speed of the microrobot (acceleration or deceleration) compared to the case where no magnetic field applied (MF-), as shown in figure 12.

3. Conclusion

In this study, the performance and modeling of a permanent magnets array actuated tumbling microrobots has been demonstrated. Both in the experiment and simulation, the microrobot was subjected to a uniform rotating magnetic field, which induced tumbling motion over the surface. The translational speed of tumbling microrobots was presented versus rotating frequency for 12 shapes of microrobots. The dynamics model of the microrobot has been demonstrated in this study, which can be used to predict the behavior of tumbling microrobots with different shapes and serve as a useful tool to guide structural design. The simulation can predict the step-out frequency for the helix structure microrobot. For some complex structures, the theoretical model can generally expect the

overall trend of the microrobot's behavior but overestimate its step-out frequency. Errors are likely due to the slippage of microrobots in practice under a higher frequency of the rotating field. For practical use, it is desirable to investigate the behavior of microrobots in vascular environments rather than steering in stagnant liquids. Our simulated results demonstrated that the tumbling microrobot could accelerate or decelerate in the bloodstream, which was beneficial for controlled active drug release.

Future works will include incorporating more accurate friction and adhesion (obtained from experiments) model and consider the slippage of microrobots into the theoretical model. In addition, an autonomous feedback control system will be investigated, which can lead to the precise deliver of the microrobot to the final target destination. The motion of the microrobot in a flow biofluid environment will also be examined.

Data availability statement

All data that support the findings of this study are included within the article (and any supplementary files).

Acknowledgments

This work was kindly supported by the United States National Science Foundation (NSF) (Award # CMMI 1851635 and # ECCS 2021081). The authors would also like to thank Mr. Yuxiang Chen from the Department of Computer Science and Software Engineering at Auburn University for providing us with the microrobot tracking code.

ORCID iDs

Jingfan Chen https://orcid.org/0000-0002-5438-4316 Ya Wang https://orcid.org/0000-0003-4353-4638

References

- [1] Purcell E M 1977 Life at low Reynolds number *Am. J. Phys.* 45 3–11
- [2] Sitti M, Ceylan H, Hu W, Giltinan J, Turan M, Yim S and Diller E 2015 Biomedical applications of untethered mobile milli/microrobots *Proc. IEEE* 103 205–24
- [3] Kim D-I, Song S, Jang S, Kim G, Lee J, Lee Y and Park S 2020 Untethered gripper-type hydrogel millirobot actuated by electric field and magnetic field *Smart Mater. Struct.* 29 085024
- [4] Mohanty S, Jin Q, Furtado G P, Ghosh A, Pahapale G, Khalil I S M, Gracias D H and Misra S 2020 Bidirectional propulsion of arc-shaped microswimmers driven by precessing magnetic fields Adv. Intell. Syst. 2 2000064
- [5] Xin C et al 2021 Environmentally adaptive shape-morphing microrobots for localized cancer cell treatment ACS Nano 15 18048–59
- [6] Bozuyuk U, Yasa O, Yasa I C, Ceylan H, Kizilel S and Sitti M 2018 Light-triggered drug release from 3D-printed magnetic chitosan microswimmers ACS Nano 12 9617–25

- [7] Ceylan H, Yasa I C, Yasa O, Tabak A F, Giltinan J and Sitti M 2019 3D-printed biodegradable microswimmer for theranostic cargo delivery and release ACS Nano 13 3353–62
- [8] Abbott J J, Peyer K E, Lagomarsino M C, Zhang L, Dong L, Kaliakatsos I K and Nelson B J 2009 How should microrobots swim? *Int. J. Robot. Res.* 28 1434–47
- [9] Wang X, Qin X-H, Hu C, Terzopoulou A, Chen X-Z, Huang T-Y, Maniura-Weber K, Pané S and Nelson B J 2018 3D printed enzymatically biodegradable soft helical microswimmers Adv. Funct. Mater. 28 1804107
- [10] Son D, Ugurlu M C and Sitti M 2021 Permanent magnet array-driven navigation of wireless millirobots inside soft tissues Sci. Adv. 7 eabi8932
- [11] Liao P, Li J, Zhang S and Sun D 2018 A fish-like magnetically propelled microswimmer fabricated by 3D laser lithography 2018 IEEE Int. Conf. on Robotics and Automation (ICRA) pp 3581–6
- [12] Jang B *et al* 2015 Undulatory locomotion of magnetic multilink nanoswimmers *Nano Lett.* **15** 4829–33
- [13] Li T *et al* 2016 Magnetically propelled fish-like nanoswimmers *Small* **12** 6098–105
- [14] Alapan Y, Bozuyuk U, Erkoc P, Karacakol A C and Sitti M 2020 Multifunctional surface microrollers for targeted cargo delivery in physiological blood flow Sci. Robot. 5 eaba5726
- [15] Lin Z, Fan X, Sun M, Gao C, He Q and Xie H 2018 Magnetically actuated peanut colloid motors for cell manipulation and patterning ACS Nano 12 2539–45
- [16] Chen W, Fan X, Sun M and Xie H 2021 The cube-shaped hematite microrobot for biomedical application *Mechatronics* 74 102498
- [17] Ahmed D, Baasch T, Blondel N, Läubli N, Dual J and Nelson B J 2017 Neutrophil-inspired propulsion in a combined acoustic and magnetic field *Nat. Commun.* 8 770
- [18] Fang W-Z, Ham S, Qiao R and Tao W-Q 2020 Magnetic actuation of surface walkers: the effects of confinement and inertia *Langmuir* 36 7046–55
- [19] Ze Q, Wu S, Nishikawa J, Dai J, Sun Y, Leanza S, Zemelka C, Novelino L S, Paulino G H and Zhao R R 2022 Soft robotic origami crawler Sci. Adv. 8 eabm7834
- [20] Pawashe C, Floyd S and Sitti M 2009 Modeling and experimental characterization of an untethered magnetic micro-robot *Int. J. Robot. Res.* 28 1077–94
- [21] Jing W, Pagano N and Cappelleri D J 2013 A novel micro-scale magnetic tumbling microrobot J. Micro-Bio Robot. 8 1–12
- [22] Bi C, Guix M, Johnson B V, Jing W and Cappelleri D J 2018 Design of microscale magnetic tumbling robots for locomotion in multiple environments and complex terrains *Micromachines* 9 68
- [23] Jang B et al 2019 Programmable locomotion mechanisms of nanowires with semihard magnetic properties near a surface boundary ACS Appl. Mater. Interfaces 11 3214–23
- [24] Suter M, Zhang L, Siringil E C, Peters C, Luehmann T, Ergeneman O, Peyer K E, Nelson B J and Hierold C 2013 Superparamagnetic microrobots: fabrication by two-photon polymerization and biocompatibility *Biomed. Microdevices* 15 997–1003
- [25] Sun H C M, Liao P, Wei T, Zhang L and Sun D 2020 Magnetically powered biodegradable microswimmers Micromachines 11 404
- [26] Ghosh A and Fischer P 2009 Controlled propulsion of artificial magnetic nanostructured propellers Nano Lett. 9 2243–5
- [27] Huang H-W, Sakar M S, Petruska A J, Pané S and Nelson B J 2016 Soft micromachines with programmable motility and morphology *Nat. Commun.* 7 12263

- [28] Taylor A P, Izquierdo Reyes J and Velásquez-García L F 2020 Compact, magnetically actuated, additively manufactured pumps for liquids and gases J. Phys. D: Appl. Phys. 53 355002
- [29] Taylor A P, Cuervo C V, Arnold D P and Velásquez-García L F 2019 Fully 3D-printed, monolithic, mini magnetic actuators for low-cost, compact systems *J. Mricomech. Syst.* 28 481–93
- [30] Li L et al 2016 Big area additive manufacturing of high performance bonded ndfeb magnets Sci. Rep. 6 36212
- [31] Kummer M P, Abbott J J, Kratochvil B E, Borer R, Sengul A and Nelson B J 2010 OctoMag: an electromagnetic system for 5-DOF wireless micromanipulation *IEEE Trans. Robot.* **26** 1006–17
- [32] Jeon S et al 2019 A magnetically controlled soft microrobot steering a guidewire in a three-dimensional phantom vascular network Soft Robot. 6 54–68
- [33] Schuerle S, Erni S, Flink M, Kratochvil B E and Nelson B J 2013 Three-dimensional magnetic manipulation of microand nanostructures for applications in life sciences *IEEE Trans. Magn.* 49 321–30
- [34] Yu J, Jin D, Chan K-F, Wang Q, Yuan K and Zhang L 2019 Active generation and magnetic actuation of microrobotic swarms in bio-fluids *Nat. Commun.* 10 5631
- [35] Peyer K E, Zhang L and Nelson B J 2013 Bio-inspired magnetic swimming microrobots for biomedical applications *Nanoscale* 5 1259–72
- [36] Chen J and Wang Y 2020 Personalized dynamic transport of magnetic nanorobots inside the brain vasculature Nanotechnology 31 495706
- [37] Baun O and Blümler P 2017 Permanent magnet system to guide superparamagnetic particles J. Magn. Magn. Mater. 439 294–304
- [38] Fischer P and Ghosh A 2011 Magnetically actuated propulsion at low Reynolds numbers: towards nanoscale control *Nanoscale* 3 557–63
- [39] Kim S, Qiu F, Kim S, Ghanbari A, Moon C, Zhang L, Nelson B J and Choi H 2013 Fabrication and characterization of magnetic microrobots for three-dimensional cell culture and targeted transportation Adv. Mater. 25 5863–8
- [40] Lee S, Kim S, Kim S, Kim J-Y, Moon C, Nelson B J and Choi H 2018 A capsule-type microrobot with pick-and-drop motion for targeted drug and cell delivery Adv. Healthcare Mater. 7 1700985
- [41] Wahajuddin W A 2012 Superparamagnetic iron oxide nanoparticles: magnetic nanoplatforms as drug carriers *Int. J. Nanomed.* 7 3445–71
- [42] Yuan M, Bancroft E A, Chen J, Srinivasan R and Wang Y 2022 Magnetic fields and magnetically stimulated gold-coated superparamagnetic iron oxide nanoparticles differentially modulate l-type voltage-gated calcium channel activity in midbrain neurons ACS Appl. Nano Mater. 5 205–15
- [43] Yuan M, Wang Y and Qin Y-X 2017 SPIO-Au core–shell nanoparticles for promoting osteogenic differentiation of MC3T3-E1 cells: concentration-dependence study *J. Biomed. Mater. Res.* A **105** 3350–9
- [44] Yuan M, Wang Y and Qin Y-X 2018 Promoting neuroregeneration by applying dynamic magnetic fields to a novel nanomedicine: superparamagnetic iron oxide (SPIO)-gold nanoparticles bounded with nerve growth factor (NGF) Nanomed.: Nanotechnol. Biol. Med. 14 1337–47
- [45] Chen J, Yuan M, Madison C A, Eitan S and Wang Y 2022 Blood-brain barrier crossing using magnetic stimulated nanoparticles *J. Control. Release* 345 557–71

- [46] Browning M B, Cereceres S N, Luong P T and Cosgriff-Hernandez E M 2014 Determination of the *in vivo* degradation mechanism of PEGDA hydrogels *J. Biomed. Mater. Res.* A 102 4244–51
- [47] Stillman Z, Jarai B M, Raman N, Patel P and Fromen C A 2020 Degradation profiles of poly(ethylene glycol)diacrylate (PEGDA)-based hydrogel nanoparticles *Polym. Chem.* 11 568–80
- [48] You S, Wang P, Schimelman J, Hwang H H and Chen S 2019 High-fidelity 3D printing using

- flashing photopolymerization *Addit.Manuf.* **30** 100834
- [49] Pieters R, Tung H W, Charreyron S, Sargent D F and Nelson B J 2015 RodBot: a rolling microrobot for micromanipulation 2015 IEEE Int. Conf. on Robotics and Automation (ICRA) pp 4042–7
- [50] Yankova G, Tur D, Parshin D, Cherevko A and Akulov A 2021 Cerebral arterial architectonics and CFD simulation in mice with type 1 diabetes mellitus of different duration *Sci. Rep.* 11 3969